ELECTRONIC, STRUCTURAL AND MAGNETIC PROPERTIES OF Co₂FeAl THIN FILMS FOR POTENTIAL SPINTRONIC APPLICATIONS

M. S. GABOR

C4S, Technical University of Cluj-Napoca
Str. Memorandumului No. 28
RO-400114 Cluj-Napoca, Romania
mihai.gabor@phys.utcluj.ro

M. BELMEGUENAI*, F. ZIGHEM and S. M. CHERIF
LSPM (CNRS-UPR 3407) 99 avenue Jean-Baptiste
Clément Université Paris 1
F-93430 Villetaneuse, France
*belmeguenai.mohamed@univ-paris13.fr

T. PETRISOR Jr and T. PETRISOR
C4S, Technical University of Cluj-Napoca
Str. Memorandumului No. 28
RO-400114 Cluj-Napoca, Romania

C. TIUSAN
Institut Jean Lamour
CNRS, Université de Lorraine
F-54506 Vandoeuvre, France

C4S, Technical University of Cluj-Napoca
Str. Memorandumului No. 28
RO-400114 Cluj-Napoca, Romania

M. HEHN
Institut Jean Lamour, CNRS
Université de Lorraine
F-54506 Vandoeuvre, France

This paper presents an overview concerning the electronic, structural and magnetic properties of Co₂FeAl (CFA) thin films. We first used *ab initio* calculations of the electronic structure in order to discuss the half-metallicity of this compound. Involving a correlated structural-magnetic

---

*Corresponding author.

analysis, we then illustrate, experimentally, the effect of the thickness as well as the annealing temperature on the magnetic and structural properties of CFA films epitaxially grown on MgO (001) single crystal substrates. The X-ray diffraction shows that in our samples having the CFA (001)[110]//MgO(001)[100] epitaxial relation, the chemical order is enhanced as the thickness and the annealing temperature (T_a) are increased. Ferromagnetic resonance measurements reveal further dynamic magnetic properties. The gyromagnetic factor, estimated at $29.2\,\mathrm{GHz/T}$, is both thickness and annealing temperature independent. The in-plane anisotropy results from the superposition between a dominant fourfold symmetry term, as expected for cubic crystal symmetry of the alloy, and a small uniaxial term. The fourfold anisotropy decreases with increasing thickness and annealing temperature. The exchange stiffness constant is thickness independent but increases with T_a. In addition, the effective magnetization varies linearly with T_a and with the inverse CFA thickness. This is due to the presence of perpendicular uniaxial anisotropy, estimated around $-1.8\,\mathrm{erg/cm^2}$ at $T_a = 600\,^\circ\mathrm{C}$ and $1.05\,\mathrm{erg/cm^2}$ at $T_a = 265\,^\circ\mathrm{C}$, respectively. Frequency and angular dependences of the FMR linewidth show two magnon scattering and mosaicity contributions which depend on the CFA thickness and T_a. A Gilbert damping coefficient as low as 0.0011 is found for samples annealed at $600\,^\circ\mathrm{C}$. Finally, we illustrate that these films can be used as ferromagnetic electrodes in sputtered epitaxial magnetic tunnel junctions (MTJ) based on MgO(001) tunnel barriers. These MTJs show an improvable TMR ratio around 95% at room temperature.

Keywords: Heusler alloys; ferromagnetic resonance; magnetization dynamics; magnetic tunnel junction; spin polarized tunneling; structural properties; magnetic properties.

1. Introduction

Spintronics is a rapidly emerging field of science and technology where electron spin is used, as well as its charge, as an information carrier. The development of spintronics was triggered by the discovery of the giant magnetoresistance (GMR) independently by Fert and Grünberg.[1,2] Thereafter, the field of spintronics showed a continuous expansion while several other effects, such as tunnel magnetoresistance (TMR)[3] and spin transfer torque (STT)[4] have been discovered and employed in commercial devices.

Nowadays, the spintronics is facing a series of challenges. First, the large TMR effect in magnetic tunnel junctions, elementary bricks of sensors and nonvolatile magnetic random access memories (MRAM), has to be continuously increased to provide adequate signal-to-noise ratios in increasingly smaller devices. Second, the critical current density for the STT magnetization switching,[5] which is proportional to Gilbert damping constant α and to the inverse of the spin polarization, should be further reduced. This is essential for applications concerning magnetization reversal by STT in STT-MRAM and for building high efficiency spin torque oscillators. Thirdly, the injection and detection of spin-polarized currents from metallic ferromagnets into semiconductors is another challenge for

spintronics due to the conductivity mismatch between the two types of materials.[6,7] This last issue can be solved by employing tunnel injectors with large spin polarization and properly tuned electrical transparency.[8]

At a first glance, a key technology which would solve all this challenges would be based on materials with high spin polarization and low damping parameters. However, the damping level has to be optimally adjusted to face other important challenge related to the engineering of the new generation of recording devices. Due to the low resistance of nanoscopic scale pillars, all metal current-perpendicular-to-plane (CPP) GMR sensors represent nowadays the ideal candidates for the ultra-high-density ($> 1\,\mathrm{Tb/in^2}$) read heads. Even if the signal level is lower than the one of a standard MgO-based TMR sensor, the lower Johnson noise of CPP-GMRs would lead to interesting signal-to noise ratios.[9] Similarly to magnetic tunnel junctions, the signal of the CPP-GMR devices can be increased by employing high polarization ferromagnetic electrodes. However, in this case the large current densities in low resistance ($< 50\,\mathrm{m\Omega \cdot \mu m^2}$) CPP-GMR pillars combined to low Gilbert damping of ferromagnetic material composing the electrodes would lead to important magnetic noise by spin-torque effects. In

order to sustain reasonable signal-to-noise ratios both polarization and damping have to be optimally adjusted. Typically, the polarization has to be maximized and the damping should be tuned appropriately.

Most of the challenges listed above can be addressed by using as ferromagnetic electrodes in spintronic devices the Heusler alloys. These materials provide a large spin polarization combined with a low Gilbert damping which can be furthermore extrinsically controlled depending on the selected spintronic application.

Heusler alloys are a special class of intermetallic compounds named after Friedrich Heusler, who in 1903 reported Cu$_2$MnAl to be a strong ferromagnet although the elemental constituents are not ferromagnetic.[10] Since the prediction of the half-metallicity, by de Groot *et al.* in 1983, of the half-Heusler alloy NiMnSb,[11] the scientific interest on Heusler alloys has been renewed and they are attracting considerable experimental and theoretical interest. In addition to NiMnSb, several other Heusler alloys have been predicted, from *ab initio* calculations, to be half-metallic, such as the Co-based full-Heusler compounds[12–14] which are promising materials for commercial spintronic applications especially due to their relative high Curie temperatures.

The full-Heusler alloys[14,15] are described by the formula X_2YZ, where X and Y are transition metals and Z is a main group *sp* element. Depending on atomic sites occupied by the X, Y and Z atoms in the elementary cell, the alloy can adopt different structures with different chemical or atomic disorder. Heusler alloys in the totally ordered phase L2$_1$ transform into the B2 structure (when the Y and Z atoms randomly share their sites). Moreover, they form an A2 structure when X, Y and Z randomly share all the sites. This chemical disorder strongly influences many of their physical properties. Indeed, it is reported by Picozzi *et al.* that some types of disorder might lead to additional states at the Fermi level, thus reducing the spin polarization.[13]

Motivated by the above-mentioned challenges, research on integrating half-metallic Heusler alloys into GMR and TMR thin film heterostructures is in progress. Based on their theoretically predicted half-metallicity, it is expected that the use of the Heusler alloys should lead to huge magnetoresistance values. However, in order to obtain experimentally the half-metallicity one has to surmount two challenges: achieving the perfect chemical and crystallographic

order, i.e., crystallization of the Heusler electrode in L2$_1$ structure and coherent interfaces of the Heusler compound and the metallic (CPP-GMR device) or MgO(001) tunnel barrier (TMR device). In this last case, of single crystal MTJs based on Heusler alloys and (001) MgO tunnel barriers, the tunnelling polarization could be particularly large due to symmetry dependent attenuation rate of propagative Bloch function selected in the single crystal ferromagnetic electrodes.[16] Therefore, even for a nonperfect half-metallic Heusler electrode, the half-metallicity could be recovered by suppression of conduction channels with large attenuation across the single crystal MgO(001) barrier. Although the obtained values are still below the theoretical expectations, relatively large TMR ratios have been reported in magnetic tunnel junctions employing Co-based full-Heusler alloys such as Co$_2$FeAl (CFA),[17–19] Co$_2$MnSi,[20–22] Co$_2$FeAl$_{0.5}$Si$_{0.5}$[23–26] and Co$_2$(Cr$_{1-x}$Fe$_x$)Al.[27] Furthermore, Co$_2$FeAl is a very attractive material due its high T_C ($T_C \approx 1000$ K)[15] and its ability to grow epitaxially on MgO surfaces and therefore high TMR ratio is expected. Indeed, a TMR ratio of 360% has been achieved in CoFe/MgO/Co$_2$FeAl structures.[17,18] In addition to its lowest magnetic damping parameter among Heuslers, as we will illustrate here, the relatively small lattice mismatch between MgO(001) and CFA(001) enables the fabrication of a high-quality CFA/MgO (001) epitaxial heterostructure for low-RA MTJs, which are essential to the observation of spin-transfer switching. In fact, spin-transfer magnetization switching using magnetic CFA-based tunnel junctions has been demonstrated[28] using intrinsic critical current density (7.1 MA/cm^2) as small as that reported one for CoFeB/MgO/CoFeB. Moreover, as we will show in this paper perpendicular magnetization of CFA full-Heusler ultra thin films can be achieved which makes CFA an ideal candidate as a ferromagnetic electrode for perpendicular MTJs. This is promising for further reduction in the critical current density of current induced magnetization switching.[4,29]

Faced to all the challenges listed above, the integration of CFA as a ferromagnetic electrode in a spintronic device requires a good knowledge allowing for a precise control of its chemical, structural, electronic, static and dynamic magnetic properties. Issued from combined theoretical and experimental studies, the main goal of this paper is to provide an overview of the electronic structure, structural,

static and dynamic magnetic properties of Co_2FeAl such as saturation magnetization, magnetic anisotropy, the exchange stiffness parameter, the gyromagnetic factor and the damping mechanisms monitoring its dynamic behavior. Both the effect of annealing temperature and thickness are investigated. Finally, we will discuss some potential applications of CFA in MTJ devices.

2. Electronic Structure

In order to get a deeper understanding of electronic structure of the CFA full-Heusler alloy, we have employed *ab initio* band structure calculations using the Wien2k code.[30] A first step was the calculation of the bulk electronic structure. The unit cell structure has been generated using the space group number 225 corresponding to Fm-3 m crystalline structure. The Wyckoff positions of the atoms are Co(1/4,1/4,1/4) (3/4,3/4,3/4), Fe(1/2,1/2,1/2) and Al(0 0 0), which correspond to the totally ordered $L2_1$ phase of CFA. Here, we considered only the situation of a perfectly ordered alloy and disregarded the A2 and B2 disordered configuration, although they have a strong impact on the spin polarization, as shown for example by Picozzi *et al.*[13]

Our simplified choice has been motivated by the purpose of our calculation. We sought to show the appearance of the half-metallic gap and to investigate the orbital character of the bands lying above and below this minority gap, especially their symmetries. This analysis in terms of symmetry is particularly important for CFA/MgO single crystal MTJs where the crystalline MgO barrier provides symmetry dependent attenuation rates. This filtering effect in terms of Bloch wave symmetry will have a major impact on the tunneling density of states and therefore on the tunneling polarization. We stress that in a tunnel junction the pertinent quantity to describe the polarization is the tunnel density of states (TDOS) and not the electrode density of states (DOS). The TDOS takes into account also the probability that a state available in DOS to propagate by tunneling across the barrier.

The lattice parameter used in our calculation has been the experimental one for CFA, $a = 0.573$ nm. Then, we relaxed the structure in order to find the equilibrium lattice parameter which minimizes the total energy of the system, as required within the local spin density approximation (LSDA) used by Wien2k. The equilibrium theoretical lattice parameter was found to be equal to $a_{min} = 0.57034$ nm. The relaxation has been done by varying isotropically with 20% the volume of the unit cell around the experimental volume.

It has been shown[31–33] that for the related Co_2FeSi compound it is necessary to include on-site correlations in the calculations in order to explain the experimental found saturation magnetization. The Hubbard correlation term U in the LSDA + U scheme is designed to model localized states when on-site Coulomb interactions become important. It is clear that the d electrons are delocalized in metals. However, since the Co based Heusler compounds follow rigorously the Slater–Pauling curve, they are generally thought of as systems that exhibit localized magnetic moments.[14] Therefore, the inclusion of electron–electron correlations might be necessary in order to respect a partial localization of the d electrons in the Heusler alloys. Therefore, we proceed as Ref. 14 and calculated the electronic structure of the CFA alloy by introducing the Hubbard correlation term U of about 2 eV.

In order to identify the nature of the minority states lying near the Fermi level (E_F), we calculated the orbital projected DOS of different atoms: Co, Fe and Al. Figure 1 summarizes our results. We regrouped the orbital character chosen for the projection to the ones belonging to the Δ_1 symmetry (e.g., s, p_z, d_z^2). These orbitals are known to be the less attenuated by an MgO single crystal barrier and therefore the wave functions with the Δ_1 symmetry will determine the dominant channels for electron tunneling across the MgO. One can immediately observe that the half-metallic minority gap is perfectly defined and extends below and above E_F for both projected electron symmetries, for Co, Fe and Al atoms.

In order to get deeper understanding on the effect of the correlations on the electronic structure of CFA, we have performed the same calculations without taking into account the Hubbard term. Figure 2 shows the projected DOS with d_z^2 character for Co, Fe and Al atoms, which are most influenced by the correlations. It can be clearly distinguished that one band (reflected by the DOS), belonging to the Fe atoms, is emerging just above the Fermi level. By hybridization, Fe–Al are lying in the same plane in the $L2_1$ structure, one can observe the presence of d-like states also on Al sites. It can be easily understood that the proximity of these minority d-like states to the Fermi level would have detrimental
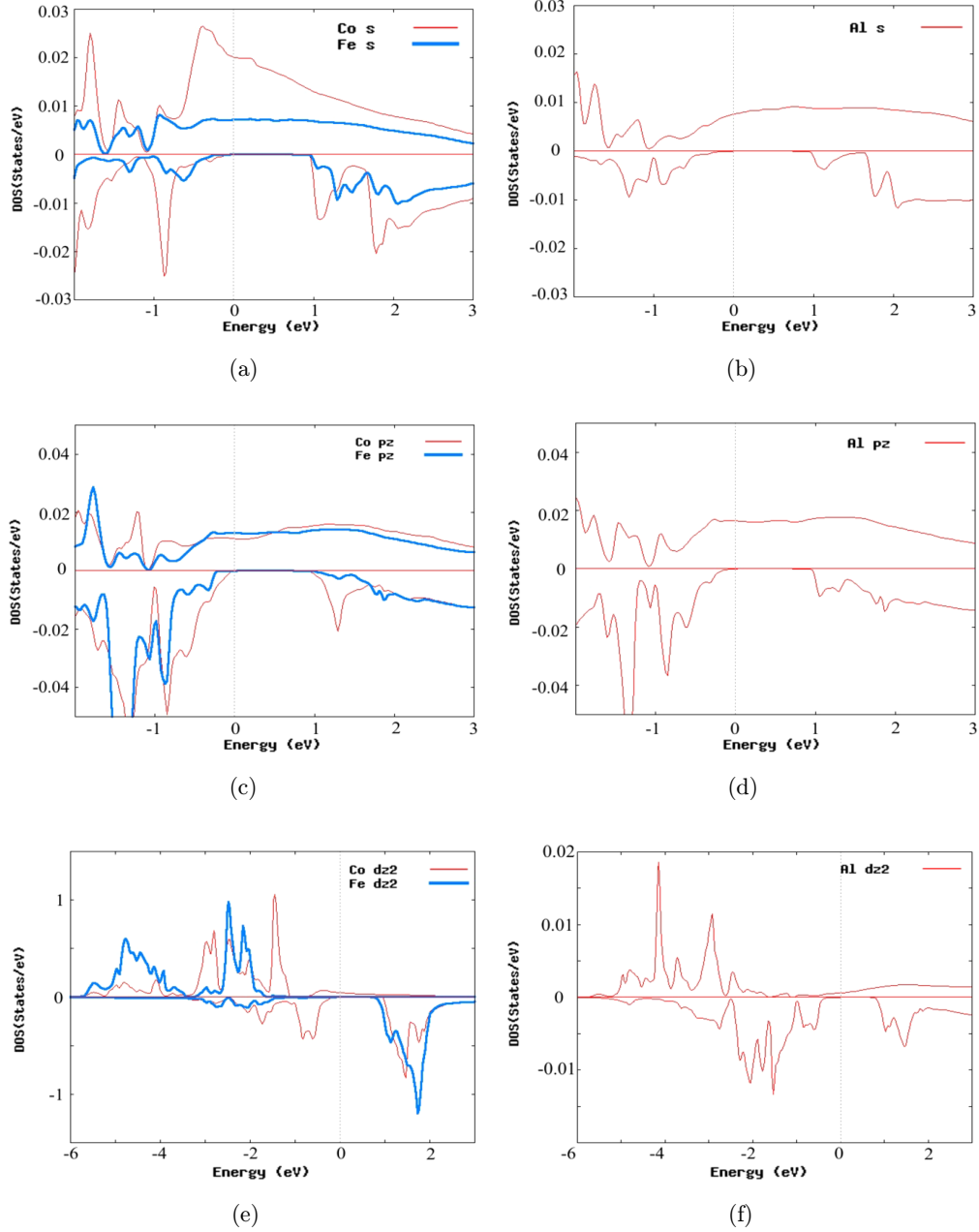
Fig. 1. (a) Projected DOS with s character for Co and Fe. (b) Projected DOS with s character for Al. (c) Projected DOS with p_z character for Co and Fe. (d) Projected DOS with p_z character for Al. (e) Projected DOS with d_z^2 character for Co and Fe. (f) Projected DOS with d_z^2 character for Al. The calculations have been performed within the LSDA + U approximation considering a Hubbard correlation term $U = 2\,\mathrm{eV}$ (color online).

effect on the tunneling polarization of the CFA Heusler. However, as can be seen from Fig. 1 by introducing the Hubbard term in the calculations the minority gap is clearly opened up and the Fermi level becomes relatively far from the gap edges. These results stress the importance of the localization of d electrons in the appearance of the minority spins gap.

In order to get deeper insight into the electronic structure of the ordered CFA alloy, especially if one wants to build MTJs where the tunnel transport takes place along the (001) direction, we calculated also the energy bands $E(k)$ as presented in Fig. 3. We compare the result of our calculation with or without introducing the Hubbard correlation term U. The comparison is meant to observe which would
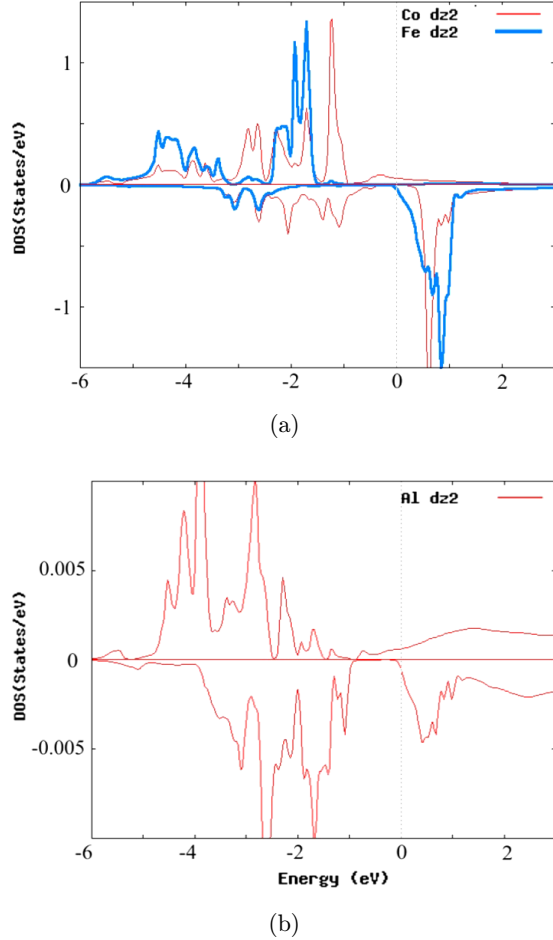
(a)

(b)

Fig. 2. (a) Projected DOS with d_z^2 character for Co and Fe. (b) Projected DOS with d_z^2 character for Al. The calculations have been performed within the LSDA approximation without taking into account the Hubbard correlation term U (color online).
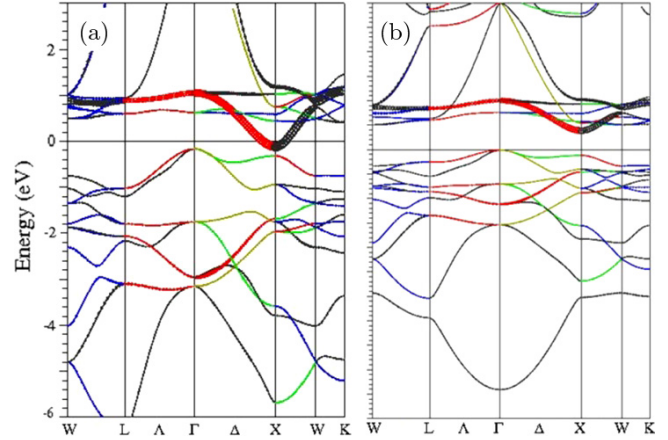

Fig. 3. Fat bands calculations for the CFA minority spin in LSDA + GGA (a) and LSDA + U approach (b). The fat bands represent energy bands which take into account the orbital character of the states. The width of the band is proportional to the amount of the orbital character of the orbital projected state in a given k point (pure states exist only in the high symmetry points, elsewhere the states have mixed character which evolves along the band dispersion in k) (color online).

be the effect of considering the correlation term U on the band structure. From the band structures, one can clearly see that the correlations have a direct effect on the increase of the minority gap width.

If one focuses around the X point following the $\Gamma\Delta X$ direction, within the LSDA + GGA approach which neglects the correlations, we observe the d_z^2-like minority bands around the Fermi level closing the minority gap. When the correlations are considered, these d_z^2 bands will be shifted about $1\,\mathrm{eV}$ above the E_F, reconstructing the half metallicity of the system. We especially focused on the bands structure along $\Gamma\Delta X$ direction in order to understand the tunneling transport in CFA/MgO single crystal junctions, where the tunneling current is dominated by the propagation of the Δ_1 states.[16]

From the fat bands analysis, one can clearly observe once more that, in the case of the LSDA + GGA approach, the minority band around the X point has d_z^2 orbital character. This is of extreme importance because the propagation of this band by tunneling is highly favored across the MgO(001), having in view that d_z^2 belongs to highly conductive Δ_1 states. However, one has to take into account that by introducing the correlations (LSDA + U) these d_z^2 bands will be shifted upward in energy, opening the minority spin gap. This clearly indicates the major effect of the electron correlations on the width of the gap and therefore of the half-metallicity of the compound.

In realistic systems, disorder will affect the gap of the minority spin. It will induce energy levels within the minority spin band gap, around the Fermi level. As a consequence, the half-metallic character will be damaged and the spin polarization reduced.[13] Nonetheless, the couple CFA(001)/MgO(001) would be expected to provide large TMR effects by recovering the half-metallicity of the Heusler in terms of tunneling polarization due to the symmetry filtering properties of the MgO tunneling barrier. An interesting feature of the band structure of the CFA is that the *worst* high symmetry direction for the half-metallic character is exactly the $\Gamma\Delta X$ direction which is the least attenuated in tunneling

propagation across the MgO (001) insulator. However, the better half-metallicity (larger gap) along the other high symmetry directions will eliminate any parasitic contribution of tunneling electrons with $k_\parallel \neq 0$.

3. Experimental Methods

CFA films were deposited on MgO (001) single-crystal substrates using a magnetron sputtering system with a base pressure lower than 3×10^{-9} Torr. Prior to the deposition of the CFA films a 4 nm thick MgO buffer layer was grown at room temperature (RT) by rf sputtering from a MgO polycrystalline target under an argon pressure of 15 mTorr. The MgO buffer layer improves the flatness quality of the substrate and traps the residual carbon, thus preventing carbon diffusion across the stack during subsequent annealing stages. After the buffer layer deposition, CFA films with different thicknesses were dc sputtered at RT from a 2 in. diameter stoichiometric target (Co50%Fe25% Al25%) under 1.0 mTorr of Ar, at a rate of 0.1 nm/s. Finally, the CFA films were capped with a MgO (4 nm)/Cr(10 nm) or with a MgO(4 nm)/Ta(10 nm) bilayer. After the growth of the stack, the structures were *ex situ* annealed during 15 min in vacuum.

Two kinds of samples will be considered here: the first group having $t = 50$ nm CFA thin films annealed at different temperatures (T_a: 315°C, 415°C, 515°C and 615°C) and caped with MgO (4 nm)/Ta(10 nm) is devoted for the investigation of the effect of the T_a on the structural and the magnetic properties. For the second set of samples, CFA thin films of variable thicknesses (10 nm $\leq t \leq$ 115 nm) have been annealed at 600°C for the investigation of the thickness dependence of the correlation between their structural and magnetic properties.

The structural properties of the samples have been analyzed by X-ray diffraction (XRD) using a high-resolution four-circle diffractometer. The static magnetic characteristics were investigated by vibrating sample magnetometry and the dynamic properties were studied using microstrip ferromagnetic resonance and Brillouin light scattering in some cases.

It should be mentioned that some data from Secs. 4 and 5 were presented in a different form, in Refs. 34 and 35.

4. Structural Properties

In order to determine the crystal structure of the CFA films, we performed XRD experiments. Figure 4 shows the X-ray $2\theta - \omega$ (out-of-plane) diffraction patterns recorded for a 50 nm thick CFA film annealed at different temperatures. An analysis of the XRD patterns illustrates that, in addition to the peak corresponding to the MgO substrate, all the samples exhibit only the (002) and (004) peaks of the CFA. This indicates a (00l) textured growth of the films. The X-ray $2\theta - \omega$ measurements alone can prove only the out of plane texture of the films. In order to confirm the epitaxial growth, ϕ-scan measurements must be employed. Figure 5 shows ϕ-scan measurement of the CFA (022) and MgO (022) reflections, performed for the 50 nm thick film
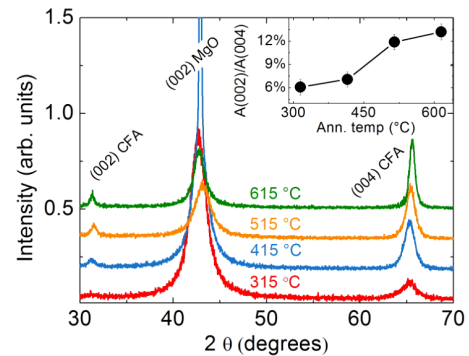

Fig. 4.   (a) X-ray $2\theta - \omega$ diffraction pattern for the 50 nm CFA thick films grown on MgO substrate annealed at different temperatures. The inset shows the evolution of the integral intensities of the (002) and (004) CFA peaks A(002)/A(004) with respect to the annealing temperatures (color online).
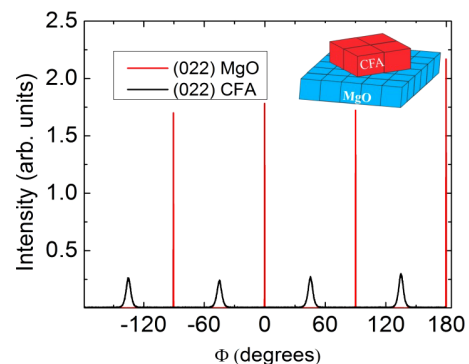

Fig. 5. ϕ-scans for CFA(022) and MgO(022) type reflections for the film annealed at 615, showing the CFA epitaxy on MgO with a 45° rotation of the CFA lattice with respect to the MgO, following the Co₂FeAl (001)[110]//MgO(001)[100] epitaxial relation. The inset shows a schematic representation of the epitaxial growth of CFA on MgO (color online).

annealed at 615°C. The ϕ-scans for the (022) CFA and MgO reflections were measured at a tilt angle $\Psi = 45°$. The four-fold symmetry of the (022) CFA reflections indicates that the films are indeed in plane oriented. The ϕ position of the CFA (022) type reflections are 45° separated from the MgO ones, confirming a 45° in-plane rotation of the CFA lattice with respect to the MgO one (Fig. 5) and the CFA(001)[110]//MgO(001)[100] epitaxial relation.

From the chemical order point of view, the CFA crystal may be in the perfectly chemically ordered L2$_1$ phase, the B2 phase characterized by disorder between Fe an Al while Co atoms occupy regular sites, and the A2 phase in which Fe, Al and Co occupy randomly the atomic sites. The perfectly ordered L2$_1$ structure is characterized by the presence of superlattice reflections such as (111) or (311).[36] In the limit of the measurements resolution, we did not observe such superlattice reflections and concluded with the absence of the L2$_1$ phase in the studied films. In contrast, the (002) superlattice peak which is characteristic to the B2 is observed. Since the (004) reflection is a fundamental one belonging to the cubic structure and does not depend on the chemical order, the integrated peak intensity ratio A(002)/A(004) represents a measure of the degree of order on Co sites. This ratio, shown in the inset of Fig. 4, increases with T_a. This indicates a monotonous evolution of the chemical order from the A2 towards the B2 phase as the T_a is increased.[37]

The XRD patterns of the CFA thin films of various thickness and annealed at 600°C are shown in Fig. 6. As expected, the measurements indicate the epitaxi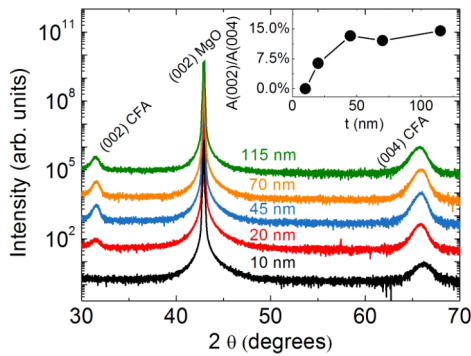al growth of the CFA films with different thicknesses. This is furthermore confirmed by pole figure measurements (not shown here). No L2$_1$ superlattice reflections were observed, regardless of the CFA film thickness. Interestingly, the integrated peak intensity ratio A(002)/A(004), which is displayed in the inset of Fig. 6 shows an increase with the thickness of the CFA layer. This indicates a transition from the A2 order towards the B2 as the thickness of the CFA layer is increased above 10 nm.

From the above presented results, we have concluded that for a constant thickness of 50 nm of the CFA layer, while the annealing temperature is increased, the chemical ordering improves from the A2 phase towards the B2 one. At the same time, for a constant annealing temperature of 600°C the chemical ordering improves by increasing the CFA film thickness. Regardless of the CFA layer thickness and annealing temperature, the L2$_1$ chemical ordering was not evidenced in our films.

5. Magnetic Dynamic Properties

All the measurements presented here were performed at room temperature using a vibrating sample magnetometer for the magnetization at saturation and a home-made microstrip ferromagnetic resonance setup (MS-FMR)[34] for the dynamic magnetic investigations. The g value, which determines the gyromagnetic factor (γ), the magnetic anisotropy, the effective magnetization, the exchange stiffness constant and other parameters are precisely accessible by the MS-FMR technique, through the study of the frequency variation versus the amplitude and the direction of the applied magnetic field. Therefore the magnetic parameters and the different relaxation mechanisms involved in the FMR linewidth broadening in CFA thin films were precisely derived at room temperature from MS-FMR measurements. Their variation versus the annealing temperature and the CFA thickness will be discussed below.

The MS-FMR measurements have been analysed using a model based on the following energy density:

Fig. 6. X-ray $2\theta-\omega$ diffraction pattern for CFA films of different thicknesses annealed at 600°C. The inset shows the evolution of the integral intensities of the (002) and (004) CFA peaks A(002)/A(004) with respect to the CFA films thickness (color online).

$$E = -M_s H[\cos(\varphi_M - \varphi_H)\sin\theta_M\sin\theta_H$$
$$+ \cos\theta_M\cos\theta_H]$$
$$- \frac{1}{2}[1 + \cos 2(\varphi_M - \varphi_u)]K_u\sin^2\theta_M$$
$$- (2\pi M_s^2 - K_\perp)\sin^2\theta_M$$
$$- \frac{1}{8}[3 + \cos 4(\varphi_M - \varphi_4)]K_4\sin^4\theta_M. \quad (1)$$

In the above expression, θ_M and φ_M represent the out-of-plane and the in-plane (referring to the substrate edges) angles defining the direction of the magnetization M_s. φ_u and φ_4 define the angles between an easy uniaxial planar axis or an easy planar fourfold axis with respect to this substrate edge. K_u, K_4 and $K_\perp$ are in-plane uniaxial, fourfold and out-of-plane uniaxial anisotropy constants, respectively. We define

$$H_u = \frac{2K_u}{M_s} \quad \text{and} \quad H_4 = \frac{4K_4}{M_s}$$

as the in-plane uniaxial and the fourfold anisotropy fields and we introduce the effective magnetization $M_{\text{eff}} = H_{\text{eff}}/4\pi$ obtained by:

$$4\pi M_{\text{eff}} = H_{\text{eff}} = 4\pi M_s - \frac{2K_\perp}{M_s} = 4\pi M_s - H_\perp. \quad (2)$$

As experimentally observed, the effective perpendicular anisotropy term $K_\perp$ is thickness dependent. $K_\perp$ describes an effective perpendicular anisotropy term which writes as: $K_\perp = K_{\perp v} + 2K_{\perp s}/t$, where $K_{\perp s}$ refers to the perpendicular anisotropy term of the interfacial energy density and the factor 2 is due to the equal contribution of both MgO interfaces with CFA.

The resonance expressions for the frequency of the uniform precession mode and for the perpendicular standing spin waves (PSSWs) modes assuming in-plane or perpendicular applied magnetic fields are given in Ref. 34. The experimental results concerning the measured peak-to-peak FMR linewidths ΔH^{PP} are analyzed in this work taking account of both intrinsic and extrinsic mechanisms. As discussed in Ref. 34, the observed magnetic field linewidth (ΔH^{PP}) is analyzed by considering Gilbert (ΔH^{Gi}),[38] mosaicity (ΔH^{mos}),[39] inhomogeneities (ΔH^{inh}) and two magnon scattering (ΔH^{2mag})[40] contributions.

5.1. *Anisotropy and exchange stiffness constant*

5.1.1. *Effect of annealing temperature*

The magnetization at saturation (not shown here) increases slightly (10% of change) with the increasing annealing temperature indicating the improvement of atomic order. A maximum value of 1029 emu/cm^3 has been achieved for the film annealed at 615°C.

The typical MS-FMR angular dependence of the resonance field at 7 GHz driven frequency of 50 nm CFA thick films annealed at 415°C, 515°C and 615°C are shown in Fig. 7(a) for the uniform precession mode. It shows that the angular behavior of the resonance field is governed by a superposition of small uniaxial, traduced by a different resonance fields at 0° (180°) and 90° (270°), and dominated fourfold anisotropies having parallel easy axes: their common axis coincides with one of the substrate edges and, consequently, with one of the $\langle 110 \rangle$ crystallographic directions of the CFA. The epitaxial symmetry properties shown in Fig. 5 agree
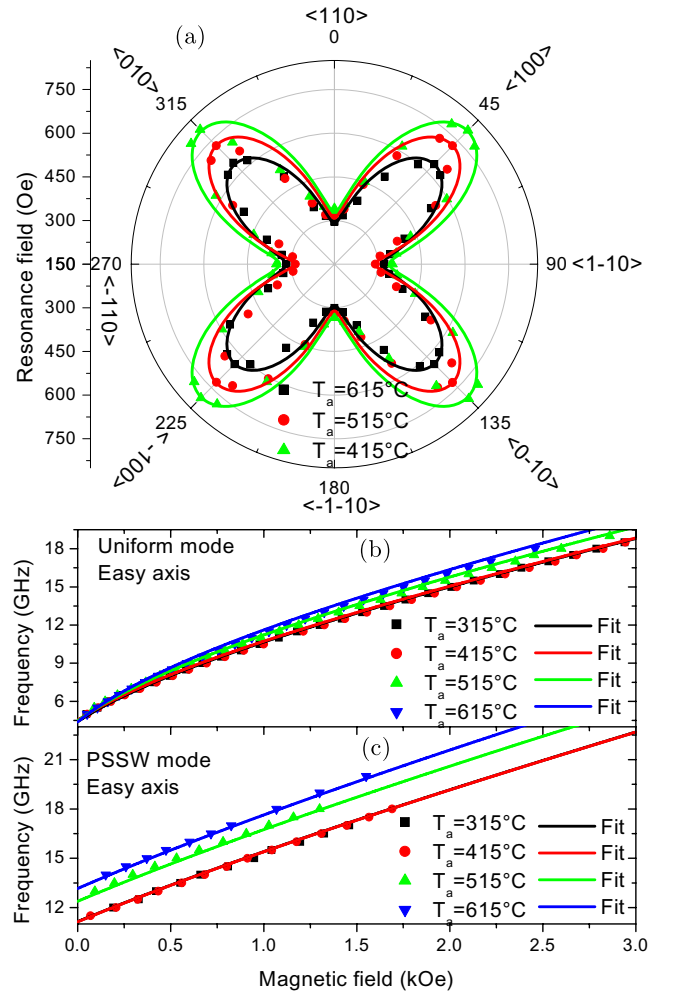

Fig. 7. (a) Polar representation of the angular dependence of the resonance field of the uniform precession mode at 7 GHz and field dependences of the resonance frequency of (b) the uniform precession and (c) the first PSSW modes of 50 nm thick Co$_2$FeAl films annealed at various temperatures. The magnetic field is applied in the film plane. The fits are obtained using model described in Ref. 34 with the parameters depicted in Fig. 8 (color online).

with the principal directions of the four-fold contribution suggesting a magnetocrystalline origin of the four-fold anisotropy, while the origin of the uniaxial anisotropy remains unclear.

The corresponding field dependence of the frequencies of the uniform precession and the first PSSW modes recorded for an applied field along the easy axis of CFA thin films annealed at various T_a are shown in Figs. 7(b) and 7(c), respectively. By fitting the data in Fig. 7 to the above-summarized model (see Ref. 34 for more details), the gyromagnetic factor (γ), exchange stiffness constant (A_{ex}), the in-plane anisotropy fields and the effective magnetization ($4\pi M_{eff}$) are extracted and the obtained values are presented in Fig. 8.
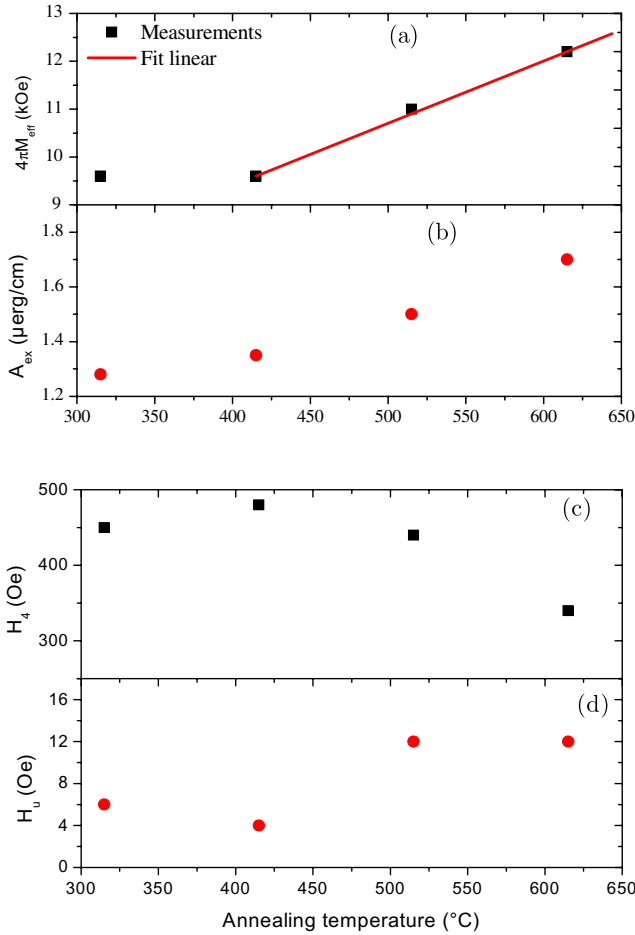

Fig. 8. Variations of (a) the effective magnetization ($4\pi M_{eff}$), the (b) exchange stiffness constant (A_{ex}), (c) the fourfold anisotropy field (H_4) and (d) the uniaxial anisotropy field (H_u) as function of the annealing temperature of 50 nm thick Co_2FeAl films grown on MgO substrates. The solid lines refer to the linear fit in the range 415–615°C.

The gyromagnetic factor ($\gamma/2\pi = 29.2$ GHz/T) is independent on T_a while A_{ex}, shown in Fig. 8(b), increases with an increasing T_a, in concordance with the enhancement of the chemical order with the increase of the annealing temperature. A similar behaviour of the exchange stiffness of $Co_2FeAl_{0.5}Si_{0.5}$ with T_a has been reported by Trudel et al.[41] Moreover, while the uniaxial anisotropy field (H_u), shown in Fig. 8(d) with an error bar of 1 Oe, does not follow a regular behavior with T_a and seems to have higher values at higher T_a, the fourfold anisotropy field (H_4) decreases as the T_a increases [Fig. 8(c)], most likely due to the improving crystalline structure and chemical order. The extracted effective magnetization from the MS-FMR measurements is shown in Fig. 8(a). It increases linearly with the annealing temperature, in the range 415–615°C, with the rate of 13 Oe/°C leading to a negative perpendicular anisotropy, which tends to favor the in-plane orientation. The origin of this anisotropy will be discussed below.

5.1.2. *Effect of the CFA thickness*

The uniform precession and the first PSSW modes have been observed in perpendicular and in-plane applied field configurations for samples thicknesses down to 45 nm. For the thickest film (115 nm), it was even possible to observe the second PSSW. For lower sample thickness, the PSSW modes are not detected due their high frequencies over-passing the available bandwidth (0–24 GHz). The angular and the field dependence of the frequency of PSSW and uniform precession modes are illustrated in Fig. 9, respectively for the 70 nm thick and for various Cr-capped CFA films.

As noticed above, the angular behavior is governed by a superposition of uniaxial and four-fold anisotropy terms with the above-mentioned easy axes with symmetry properties in agreement with the principal epitaxial directions of the growth. The conjointly fit of MS-FMR results shown in Fig. 9 using the measured VSM magnetization at saturation averaged upon all the investigated samples ($M_s = 1000 \pm 50$ emu/cm^3) revealed that γ and A_{ex} values are 2.92 GHz/kOe and 1.5 μerg/cm, respectively. This value does not depend on the studied sample.

The four-fold and the uniaxial anisotropy fields extracted from the fit of the experimental data using the above-summarized model (see Ref. 34 for more
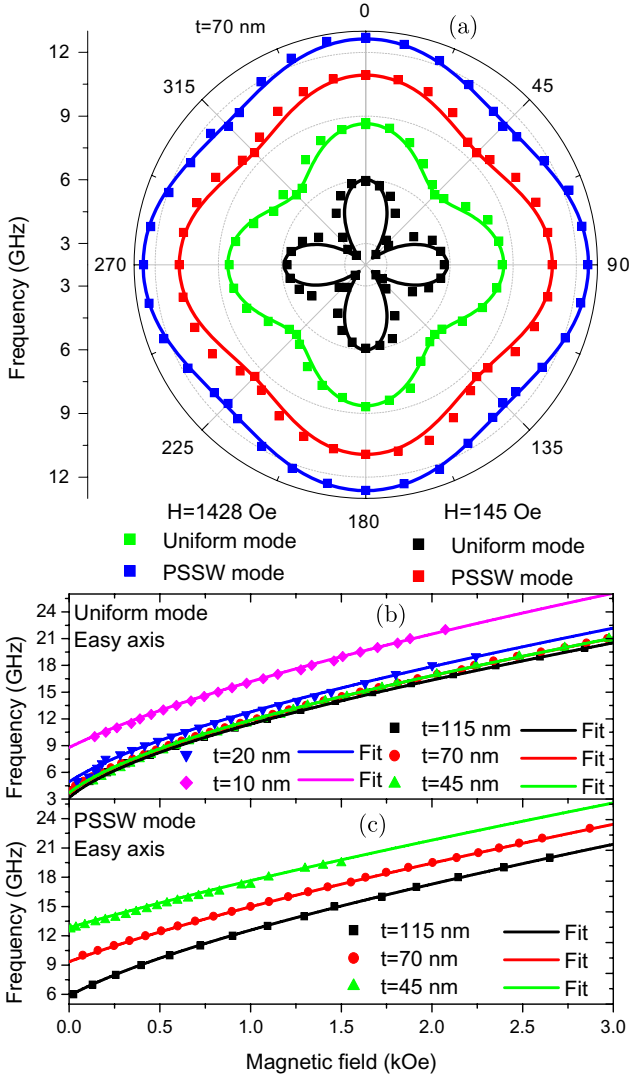
Fig. 9. (a) Angular and (b), (c) field dependences of the frequencies of the uniform precession and the PSSW modes of Co$_2$FeAl of various thickness t annealed at 600°C. The magnetic field is applied in the film plane. The fits are obtained using model described in Ref. 34 with the parameters described in Fig. 10 (color online).

Fig. 10. Thickness dependence of (a) the uniaxial (H_u), the fourfold anisotropy fields (H_4) and (b) the effective magnetization ($4\pi M_{eff}$) extracted from the fit of FMR measurements of CFA thin films annealed at 600°C. The solid lines are the linear fits (color online).

details) are shown in Fig. 10(a). For all the samples, the four-fold anisotropy is dominant. While the uniaxial anisotropy field (H_u) of the Cr-capped films is small and does not seem to depend upon the thickness, H_u is higher for the Ta-capped films, maybe due to interface effects, and is a decreasing function of the thickness [Fig. 10(a)]. Up to now we have no completely satisfying interpretation of the presence of H_u and of its variations versus the nature of the film capping. The four-fold anisotropy fields (H_4) are comparable for Cr- and Ta-capped films and decrease when their thickness increases, as
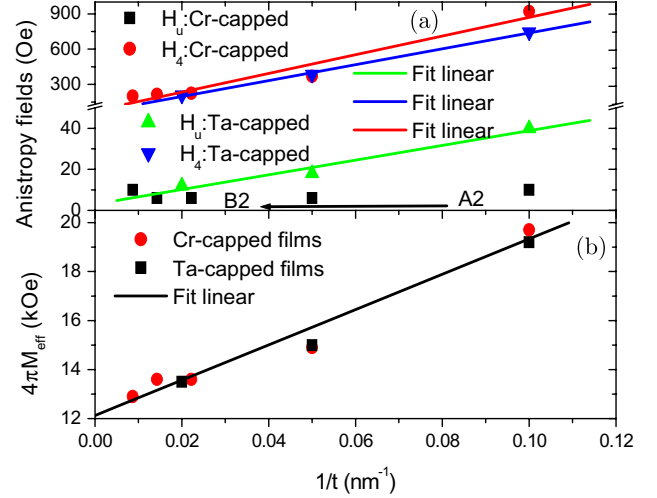
seen in Fig. 10(a) most probably due to the B2 $\Rightarrow$ A2 phase transition, observed through XRD, when the CFA thickness decreases. According to the effect of the annealing temperature, which is also attributed to the enhancement of the chemical order, it seems that the most disordered phase A2 has a higher fourfold anisotropy than the B2 one.

Figure 10(b) plots the extracted effective magnetization, $4\pi M_{eff}$, versus the film thickness $1/t$. It can be seen that M_{eff} follows a linear variation. This allows us to derive the perpendicular surface anisotropy coefficient ($K_{\perp s}$): $K_{\perp s} = -1.8 \, \mathrm{erg/cm}^2$. The limit of $4\pi M_{eff}$ when $1/t$ tends to zero is equal to 12.2 kOe, which is, within the experimental accuracy, the same as the magnetization at saturation ($4\pi M_s$). The perpendicular magnetic anisotropy, which derives from a surface effect energy term, has a negative value and provides an in-plane contribution. It originates from the CFA/MgO interface which is improving with the annealing temperature and which leads to an enhancement of the effective magnetization, as shown in Fig. 8(a). This type of thickness dependent behavior of the effective magnetization was also observed in CoFeB/MgO based structures[42] where the CoFeB/MgO interface favours a perpendicular magnetization.

It is worth to mention that for 5 nm thick samples annealed at 600°C, a lower effective magnetization has been obtained. This suggests an inverse thickness dependence trend of $4\pi M_{eff}$ for lower thickness

of CFA, which might lead to perpendicular magnetic easy axis. At least three parameters, such as, cap and buffer layers, annealing temperature and CFA thin films thickness should be tuned in order to stabilize the perpendicular magnetic anisotropy. Therefore, we have grown MgO/MgO(4)/Cr(20)/CFA(t)/MgO (0.65)/Cr(1.5) heterostructures (numbers indicate thickness in nm) of various CFA thickness ($1\,nm \leq t \leq 10\,nm$) and annealed them at $265\,°C$, in the absence of an applied magnetic field. In Fig. 11, the extracted effective magnetization M_{eff} against film thickness is plotted. One can observe that M_{eff} can be fitted linearly to the inverse of CFA film thickness in the range 1.8–1 nm. The M_{eff} decreases to zero at around $t = 1.2\,nm$, below which the surface anisotropy will overcome the demagnetization field and causes the magnetic easy axis to switch out-of-plane (negative M_{eff}). This has been confirmed by the hysteresis loops of the 1.2 nm and 1 nm thick CFA films measured by polar magneto-optical Kerr effect (shown in the inset of Fig. 11). Using the above-mentioned average value of the magnetization at saturation ($M_s = 1000\,eum/cm^3$), the perpendicular surface anisotropy constant is found to be $K_{\perp s} = 1.05\,erg/cm^2$. This value is in good agreement with the value reported for MgO/Co$_{40}$Fe$_{40}$B$_{20}$/Ta/ Ru structure[43] and for other CFA/MgO-based heterostructures.[44,45]
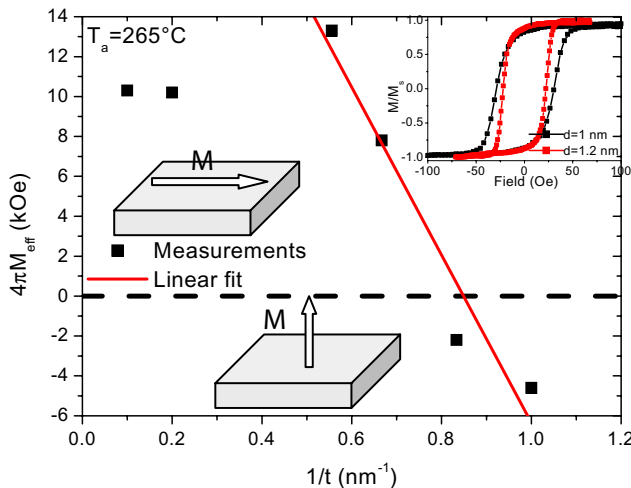

Fig. 11. Thickness dependence of the effective magnetization ($4\pi M_{eff}$) extracted from the fit of MS-FMR and Brillouin light scattering measurements of CFA thin films annealed at $265\,°C$. The inset shows the hysteresis loops, measured by Kerr effect, of 1 nm and 1.2 nm CFA thin films submitted to perpendicular applied magnetic field (color online).

5.2. *FMR linewidths*

Gilbert damping parameter controls how fast the magnetization reverses and therefore it is an important technological parameter. Although low damping is essential for spin switching with low currents and spin torque oscillators, it enhances the spin-torque-induced magnetic noise in CPP GMR sensors. The information on damping and therefore the relaxation mechanisms can be obtained by measuring the ferromagnetic resonance linewidth in the small amplitude regime. This linewidth is caused by two mechanisms: the intrinsic damping (Gilbert damping) of the magnetization and extrinsic contributions (such as two magnons scattering, mosaicity, etc.) as mentioned above. The intrinsic damping processes are the unavoidable ones and the extrinsic processes can eventually be controllable. The angular and frequency dependences of the FMR linewidth provide information about these magnetic damping mechanisms. Therefore, the field peak to peak FMR linewidth, defined as the field difference between the extrema of the sweep-field measured FMR spectra, has been investigated as function of the annealing temperature and the CFA thickness. Since the similarities between behaviours of the linewidth with thickness and T_a in our samples, their effects will be discussed together.

Figures 12(b) and 12(d) show the FMR peak to peak linewidth (ΔH^{PP}), defined as the field difference between the extrema of the FMR derivative curve, as a function of the field angle φ_H for the 70 nm and 50 nm Cr- and Ta-capped CFA films, respectively annealed at $600\,°C$ for two driving frequencies of 6 GHz and 9 GHz. For comparison, the angular dependence of the resonance fields are plotted in Figs. 12(a) and 12(c). All the other samples show a qualitatively similar behavior to one of the samples presented here. The linewidth always presents a minimum for an applied field parallel to the above-mentioned easiest axis. The positions of the maxima depend on the sample.

The observed pronounced anisotropy of the linewidth cannot be due to the Gilbert damping contribution, which is expected to be isotropic, and must be due to additional extrinsic damping mechanisms. In the 50 nm thick sample, the ΔH^{PP} angular variation shows a perfect fourfold symmetry (in agreement with the variation of the resonance position). Such behaviour is characteristic of two-magnon scattering. This effect is correlated to the
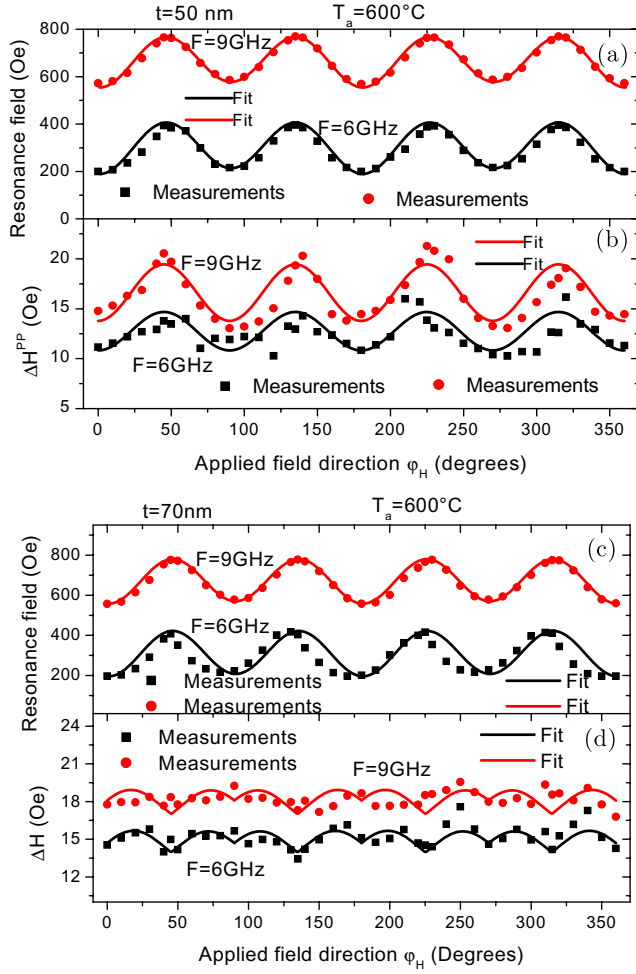
Fig. 12. Angular dependence of the resonance field and the peak to peak field FMR of 50 nm Ta-capped and 70 nm thick Cr-capped Co$_2$FeAl thin films annealed at 600°C. The solid lines refer to the fits using the mentioned models and the parameters in Ref. 34 (color online).

Fig. 13. Frequency dependence of the easy axis ($\varphi_H = 0°$) and hard axis of peak to peak field FMR linewidth (ΔH^{PP}) for Co$_2$FeAl thin (a) of different thickness annealed at 600°C and (b) 50 nm thick film annealed at various temperatures. The solid lines refer to the fit using the model described in Ref. 34 and the parameters listed in Refs. 34 and 35 (color online).

presence of defects preferentially oriented along specific crystallographic directions, thus leading to an asymmetry. Concerning the 70 nm thick film, the in-plane angular dependence of ΔH^{PP} is less simple and shows eight maxima, indicating an additional contribution driven by the mosaicity. Therefore, the entire angular dependence of the FMR linewidth in our samples can be explained as resulting of the four contributions mentioned above: two magnon scattering, mosaicity, inhomogeneities and Gilbert damping.

Furthermore, the frequency dependence of FMR linewidth, for applied fields parallel to the easy and the hard axes, for all the CFA films of various thicknesses and annealed at different temperatures presented in Fig. 13 shows that the linewidth
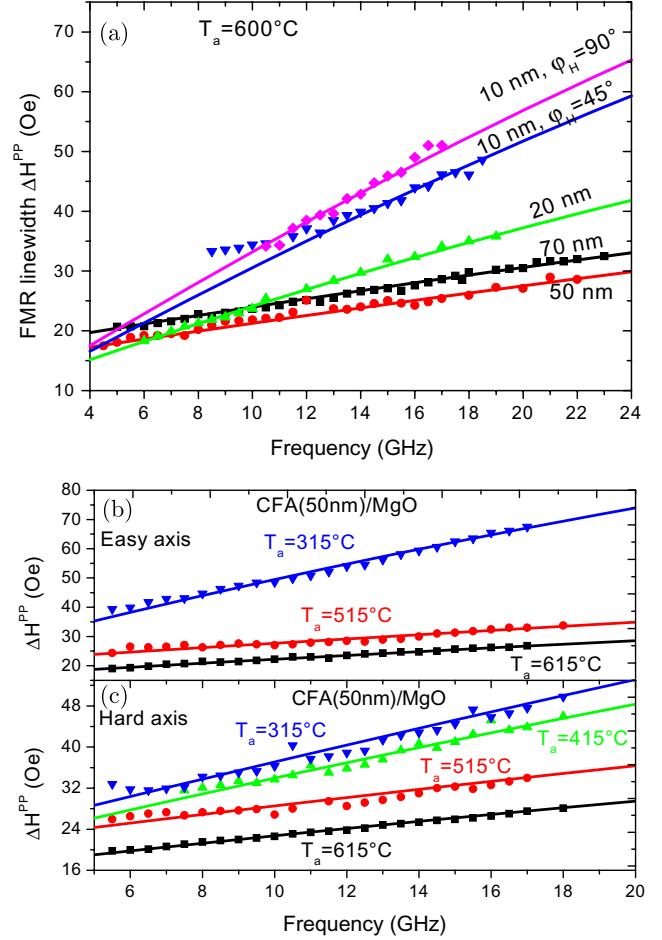
decreases with increasing T_{a} and thickness (for the Ta-capped films) due to the enhancement of the chemical order. Due to the high values of $4\pi M_{\mathrm{eff}}$ for our samples, the frequency variation of ΔH^{PP} does not allow for evidencing the existence of the two magnon contribution in contrast to its in-plane angular dependence, since the linear behavior of both Gilbert and two magnon scattering contributions according to Ref. 34. Therefore, the observed angular and frequency dependences of the field linewidth have been analyzed conjointly by considering intrinsic and extrinsic contributions, using the similar method described in Ref. 34. This analysis shows that intrinsic Gilbert coefficient is found to be independent of the studied sample and equal to 1.1×10^{-3}, in good agreement with the measured
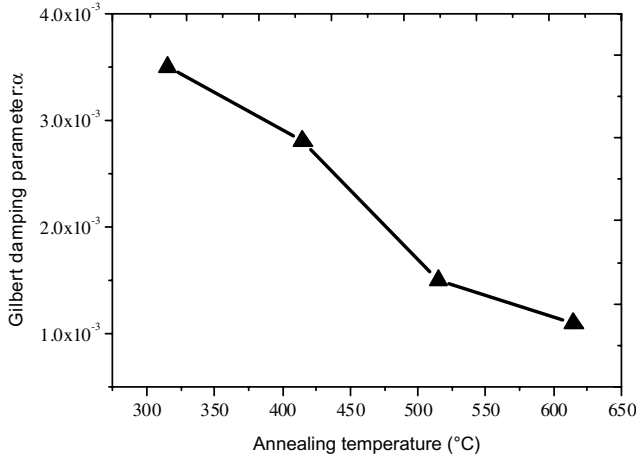
Fig. 14. Annealing temperature dependence of the Gilbert damping parameter of 50 nm CFA thin films grown MgO substrate.

value by Mizukami *et al.*[46] while it is T_a dependent as shown in Fig. 14. The reason for the decrease of α with increasing T_a is most probably due to increase of the chemical order degree[46] more affected by the annealing than by the thickness at higher annealing temperatures.

The different parameters describing the Gilbert damping, the two magnon scattering, the mosaicity and the inhomogeneity are listed in Refs. 34 and 35. The two-magnon and the mosaicity contributions to ΔH^{PP} increase when the thickness decreases, probably due to the progressive above reported loss of chemical order. Finally it is important to notice that the very low value of the intrinsic damping in the studied samples, which is comparable to that of $Fe_{0.63}V_{0.37}$ considered as the ferromagnetic metal having the lowest α[47], increases the potential application of CFA in spintronics.

6. Magnetic Tunnel Junctions with Co$_2$FeAl Electrodes Properties

The CFA films have been used as ferromagnetic electrodes in magnetic tunnel junction (MTJ) structures. The MTJ multilayer stacks have been grown by sputtering in a hard/soft architecture on single crystal MgO(001) substrates. The substrate choice has been motivated by the symmetry filtering effects across the single crystal MgO(001) barriers[16] which should provide enhanced tunneling polarization. In our stacks, the soft layer is constituted by a 30 nm thick CFA film, with in-plane magnetization (see Sec. 5.1), whereas an exchange-biased $Co_{50}Fe_{50}$

(5 nm)/IrMn(10 nm) bilayer has been used as the hard reference. After the deposition, the multilayer stack has been annealed at 350°C under an external magnetic field in order to enhance the crystalline quality of the stacks and to define a magnetic pinning direction.

In order to perform magneto-transport experiments, the MTJ stacks have been patterned by UV lithography and ion beam etching in square MTJ devices with a lateral size from $10\,\mu m$ to $50\,\mu m$. In Fig. 15, we illustrate a typical $R(H)$ curve measured at room temperature on a MTJ pillar with a MgO barrier thickness of 2.1 nm. The measured room temperature TMR ratio is around 95% which would correspond to an effective spin polarization of about 63%, according to Jullière's model.[48] These limited values with respect to theoretical expectations indicate that both the half-metallicity of CFA and the symmetry filtering efficiency by the MgO(001) are affected by some negative factors specific to realistic MTJ single crystal multilayer stacks.

To get deeper in the spin depolarization mechanisms, we have performed combined structural analysis and magneto-transport experiments in variable temperature.[49] Our analysis, accomplished on samples with thick MgO barriers, where the density of extended structural defects is enhanced, demonstrates unambiguously the detrimental effects of misfit-dislocations in a single crystal tunnel barrier on the spin polarization of tunneling electrons. Combining geometric phase analysis of High Resolution Cross Section Transmission Electron Microscopy experiments,[50] magneto-transport experiments in variable temperature and theoretical extended Glazman–Matveev fits, we demonstrate that the defects have a double impact on spin polarized tunneling. First, they
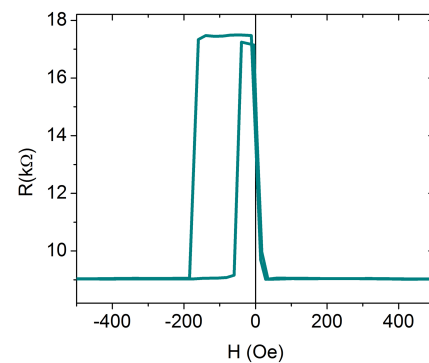

Fig. 15. Typical TMR curve measured for a MTJ with the following multilayer structure: MgO(100)/Co$_2$FeAl/MgO/Co$_{50}$Fe$_{50}$/IrMn.

destroy the longitudinal and lateral coherence of the propagating Bloch functions. This affects the efficiency of the symmetry filtering across the single crystal MgO barrier and reduces the effective spin polarization. Second, the dislocations provide localized energy levels within the MgO gap responsible on temperature activated inelastic tunneling, which explains the significant variation of TMR with the temperature.[48]

Beyond the polarization reduction by the incoherent transport across the insulator, the half metallicity of the CFA is negatively affected by other relevant factors, related to the elaboration procedure of our MTJ stacks. First, the insufficient 350°C annealing temperature of the MTJ stack does not allow the requested structural and chemical ordering and has collateral consequences in electronic and magnetic properties of the Heusler.[35] Annealing the complete MTJ stack to higher temperature would lead to diffusion of Mn, from the IrMn antiferomagnetic layer, across the interfaces and would have further negative effect on spin polarization. Second, hybridization between the CFA constituent atoms (mainly Co, Fe) and O has to be considered at the interface CFA/MgO. This, phenomenon is strongly dependent on the interface morphology and could lead to a non half-metallic surface electronic structure of CFA, very different to the bulk-one with expected half-metallic properties. A possible way to overcome some of these difficulties consists in sequential annealing of the MTJ layers during the sample elaboration in an ultrahigh vacuum sputtering system. Therefore, a first annealing step of the bottom CFA layer of a CFA/MgO/CoFe/IrMn at temperatures around 450–480°C will certainly improve its quality.[51] Then, a second annealing step of the complete stack can be performed at a lower temperature under in plane applied magnetic field. This provides the exchange bias pining of the hard layer with a limited detrimental Mn diffusion. Following this strategy, large TMR ratios (360% at RT and 785% at 10 K) have been recently reported in epitaxial CFA-based MTJs with a sputter-deposited MgO barrier.[17,18,51] These promising results underline the significant potential of the CFA to be integrated in MTJ devices with large TMR ratios originating from high spin polarization Heusler layer and strong contribution of the coherent tunneling effect through Δ_1 Bloch states in the CFA and the MgO barrier. Moreover, recently (001)-textured CFA films grown on MgO buffered Si/SiO$_2$ substrates leaded to (001) textured CFA/MgO/CoFe MTJs showing large TMR ratios[19] (166% at RT, 252% at 42 K). These textured Heusler-based MTJs grown on amorphous substrates are even more interesting for technological applications of full-Heuslers in spintronic devices with respect to those grown on single crystal MgO(001) substrates.

7. Conclusion

In this paper, we presented a detailed study dedicated to Co$_2$FeAl Heusler alloy which has important applications in spintronic devices. First, using *ab initio* electronic structure calculations we discuss the half-metallicity of this compound. A special attention has been focused on some band symmetry aspects. This is particularly important for magnetic tunnel junction applications, where the electronic Bloch states selected in the Heusler electrode tunnel with symmetry dependent attenuation rate across single crystalline MgO(001) barriers. Furthermore, the paper presents a complex study concerning the correlation between the structural, the static and the dynamic magnetic properties of Co$_2$FeAl (CFA) thin films epitaxially grown on single crystalline (001) MgO substrates. Co$_2$FeAl (CFA) films of various thicknesses ($10\,\text{nm} \leq t \leq 115\,\text{nm}$) were grown by sputtering on a (001) MgO substrate and annealed at different temperatures ($265°\text{C} \leq T_\text{a} \leq 615°\text{C}$). According to the XRD investigation, they show full epitaxial growth with chemical order varying from B2 to A2 phase as the thickness or the annealing temperature decreases. The microstrip ferromagnetic resonance (MS-FMR), used to study the dynamic properties and the anisotropy, revealed that the in-plane anisotropy presents two contributions: a four-fold and a two-fold uniaxial symmetry, respectively. The in-plane fourfold anisotropy field shows both thickness and annealing temperature dependence correlated to the thickness and annealing temperature dependence of the chemical order. The presence of the four-fold anisotropy is directly correlated to the crystalline structure of CFA grown on MgO. The effective magnetization increases drastically with decreasing CFA thickness and increasing annealing temperature, due to the enhancement of the CFA/MgO interface quality. For appropriate ultra thin CFA stacks annealed at low temperature (below 300°C), the magnetic anisotropy easy axis switches perpendicular to the film plane

M. S. Gabor et al.

due to the large positive interface anisotropy. The gyromagnetic factor is found to be independent of annealing temperature and CFA thickness while the exchange stiffness constant increases with the annealing temperature. The angular and frequency dependences of the FMR linewidth, which decreases with increasing annealing temperature and thicknesses, are governed by two magnons scattering and by a Gilbert damping which decreases with the increasing annealing temperature due to the chemical disorder. A Gilbert damping coefficient as low as 0.0011, found for samples annealed at 600°C reinforces the interest on CFA and makes it ideal material for some spintronic applications. The CFA films have been used as ferromagnetic electrode in sputtered epitaxial magnetic tunnel junctions (MTJ) based on MgO(001) barriers. These MTJs show TMR ratios around 95% at room temperature.

Acknowledgments

References

1. M. N. Baibich, J. M. Broto, A. Fert, F. N. Van Dau, F. Petroff, P. Eitenne, G. Greuzet, A. Friederich and J. Chazelas, *Phys. Rev. Lett.* **61**, 2472 (1988).
2. G. Binasch, P. Grünberg, F. Saurenbach and W. Zinn, *Phys. Rev. B* **39**, 4828 (1989).
3. J. S. Moodera, L. R. Kinder, T. M. Wong and R. Meservey, *Phys. Rev. Lett.* **74**, 3247 (1995).
4. S. Mangin, D. Ravelosona, J. A. Katine, M. J. Carey, B. D. Terris and E. E. Fullerton, *Nature Mater.* **5**, 210 (2006).
5. D. C. Ralph and M. D. Stiles, *J. Magn. Magn. Mat.* **320**, 1190 (2008).
6. H. Jaffrès and A. Fert, *J. Appl. Phys.* **91**, 8111 (2002).
7. G. Schmidt, *J. Phys. D: Appl. Phys.* **38**, R107 (2005).
8. A. Fert and H. Jaffres, *Phys. Rev. B*, 184420 (2001).
9. J. R. Childress, M. J. Carey, S. Maat, N. Smith, R. E. Fontana, D. Druist, K. Carey, J. A. Katine, N. Robertson, T. D. Boone, M. Alex, J. Moore and C. H. Tsang, *IEEE Trans. Magn.* **44**, 90 (2008).
10. F. Heusler, *Verh. Deutsch. Phys. Ges.* **5**, 219 (1903).
11. R. A. de Groot, F. M. Mueller, P. G. van Engen and K. H. J. Buschow, *Phys. Rev. Lett.* **50**, 2024 (1983).
12. I. Galanakis, P. H. Dederichs and N. Papanikolaou, *Phys. Rev. B* **66**, 174429 (2002).
13. S. Picozzi, A. Continenza and A. J. Freeman, *Phys. Rev. B* **66**, 094421 (2002).
14. H. C. Kandpal, G. H. Fecher and C. Felser, *J. Phys. D* **40**, 1507 (2007).
15. S. Trudel, O. Gaier, J. Hamrle and B. Hillebrands, *J. Phys. D* **43**, 193001 (2010).
16. W. H. Butler, X.-G. Zhang, T. C. Schulthess and J. M. MacLaren, *Phys. Rev. B* **63**, 054416 (2001).
17. W. H. Wang, E. Liu, M. Kodzuka, H. Sukegawa, M. Wojcik, E. Jedryka, G. H. Wu, K. Inomata, S. Mitani and K. Hono, *Phys. Rev. B* **81**, 140402(R) (2010).
18. W. H. Wang, H. Sukegawa and K. Inomata, *Phys. Rev. B* **82**, 092402 (2010).
19. Z. Wen, H. Sukegawa, S. Mitani and K. Inomata, *Appl. Phys. Lett.* **98**, 192505 (2011).
20. T. Ishikawa, S. Hakamata, K. Matsuda, T. Uemura and M. Yamamoto, *J. Appl. Phys.* **103**, 07A919 (2008).
21. S. Tsunegi, Y. Sakuraba, M. Oogane, K. Takanashi and Y. Ando, *Appl. Phys. Lett.* **93**, 112506 (2008).
22. H. Liu, Y. Honda, T. Taira, K. Matsuda, M. Arita, T. Uemura and M. Yamamoto, *Appl. Phys. Lett.* **101**, 132418 (2012).
23. N. Tezuka, N. Ikeda, F. Mitsuhashi and S. Sugimoto, *Appl. Phys. Lett.* **94**, 162504 (2009).
24. N. Tezuka, N. Ikeda, A. Miyazaki, S. Sugimoto, M. Kikuchi and K. Inomata, *Appl. Phys. Lett.* **89**, 112514 (2006).
25. N. Tezuka, N. Ikeda, S. Sugimoto and K. Inomata, *Appl. Phys. Lett.* **89**, 252508 (2006).
26. H. Sukegawa, W. Wang, R. Shan, T. Nakatani, K. Inomata and K. Hono, *Phys. Rev. B* **79**, 184418 (2009).
27. T. Marukame and M. Yamamoto, *J. Appl. Phys.* **101**, 083906 (2007).
28. H. Sukegawa, Z. Wen, K. Kondou, S. Kasai, S. Mitani and K. Inomata, *Appl. Phys. Lett.* **100**, 182403 (2012).
29. R. Sbiaa, S. Y. H. Lua, R. Law, H. Meng, R. Lye and H. K. Tan, *J. Appl. Phys.* **109**, 07C077 (2001).
30. P. Blaha, K. Schwarz, G. K. H. Madsen, D. Kvasnicka and J. Luitz, Wien2k, An augmented plane wave local orbitals program for calculating crystal properties (Technical University of Wien, Austria, 2001), ISBN 3-9501031-1-2.
31. H. C. Kandpal, G. H. Fecher, C. Felser and G. Schonhense, *Phys. Rev. B* **73**, 094422 (2006).
32. S. Wurmehl, G. H. Fecher, H. C. Kandpal, V. Ksenofontov, C. Felser, H.-J. Lin and J. Morais, *Phys. Rev. B* **72**, 184434 (2005).

33. Z. Gercsi and K. Hono, *J. Phys.: Condens. Matter* **19** 326216 (2007).

34. M. Belmeguenai, H. Tuzcuoglu, M. S. Gabor, T. Petrisor Jr., C. Tiusan, D. Berling, F. Zighem, T. Chauveau, S. M. Chérif and P. Moch, *Phys. Rev. B* **87**, 184431 (2013).

35. M. Belmeguenai, H. Tuzcuoglu, M. S. Gabor, T. Petrisor Jr., C. Tiusan, F. Zighem, S. M. Chérif and P. Moch, *J. Appl. Phys.* **115**, 043918 (2014).

36. P. J. Ziebeck and K. R. A. Webster, *Magnetic Properties of Metals*, eds. H. P. J. Wijn, Landolt-Bornstein, New Series, Group III, Vol. 19c, Pt. 2 (Springer-Verlag, Berlin, 1988).

37. M. S. Gabor, T. Petrisor Jr. and C. Tiusan, M. Hehn and T. Petrisor, *Phys. Rev. B* **84**, 134413 (2011).

38. B. Heinrich and J. F. Cochran, *J. Appl. Phys.* **57**, 3690 (1985).

39. D. McMichael, D. J. Twisselmann and A. Kunz, *Phys. Rev. Lett.* **90**, 227601 (2003).

40. A. K. Srivastava, M. J. Hurben, M. A. Wittenauer, P. Kabos, C. E. Patton, R. Ramesh, P. C. Dorsey and D. B. Chrisey, *J. Appl. Phys.* **85**, 7838 (2009).

41. S. Trudel, G. Wolf, J. Hamrle, B. Hillebrands, P. Klaer, M. Kallmayer, H. J. Elmers, H. Sukegawa, W. Wang and K. Inomata, *Phys. Rev. B* **83**, 104412 (2011).

42. S. Ikeda, K. Miura, H. Yamamoto, K. Mizunuma, H. D. Gan, M. Endo, S. Kanai, J. Hayakawa, F. Matsukura and H. Ohno, *Nature Mater.* **9**, 721 (2010).

43. X. Liu, W. Zhang, M. J. Carter and G. Xiao, *J. Appl. Phys.* **110**, 033910 (2011).

44. M. S. Gabor, T. Petrisor Jr., C. Tiusan and T. Petrisor, *J. Appl. Phys.* **114**, 063905 (2013).

45. Z. Wen, H. Sukegawa, S. Mitani and K. Inomata, *Appl. Phys. Lett.* **98**, 242507 (2011).

46. S. Mizukami, D. Watanabe, M. Oogane, Y. Ando, Y. Miura, M. Shirai and T. Miyazaki, *J. Appl. Phys.* **105**, 07D306 (2009).

47. C. Scheck, L. Cheng, I. Barsukov, Z. Frait and W. E. Bailey, *Phys. Rev. Lett.* **98**, 117601 (2007).

48. M. Julliere, *Phys. Lett.* **54A**, 225 (1975).

49. M. S. Gabor, C. Tiusan, T. Petrisor Jr., T. Petrisor, M. Hehn, Y. Lu and E. Snoeck, *J. Magn. Magn. Matter.* **347**, 79 (2013).

50. M. Hytch, E. Snoeck and R. Kilaas, *Ultramicroscopy* **74**, 131 (1998).

51. W. H. Wang, H. Sukegawa, R. Shan, S. Mitani and K. Inomata, *Appl. Phys. Lett.* **95**, 182502 (2009).